COMMUNICATION

Check for updates

Synthesis and symmetry of perovskite oxynitride CaW(O,N)₃†

Matthew E. Sweers, [iD] [a] Tzu-chen Liu, [iD] [a] Jiahong Shen,[a] Bingzhang Lu,[b]
John W. Freeland,[c] Christopher Wolverton, [iD] [a] Gabriela B. Gonzalez Aviles[d] and
Linsey C. Seitz [iD] *[b]

Perovskite oxynitrides, in addition to being promising electrocatalysts and photoabsorbers, present an interesting case study in crystal symmetry. Full or partial ordering of the O and N anions affects global symmetry and influences material performance and functionality; however, anion ordering is challenging to detect experimentally. In this work, we synthesize a novel perovskite oxynitride CaW(O,N)₃ and characterize its crystal structure using both X-ray and neutron diffraction. Through co-refinement of the diffraction patterns with a range of literature and theory-derived model structures, we demonstrate that CaW(O,N)₃ adopts an orthorhombic *Pnma* average structure and exhibits octahedral distortion with evidence for preferred anion site occupancy. However, through comparison with a large, low-symmetry unit cell, we identify the presence of disorder that is not fully accounted for by the high-symmetry model. We compare CaW(O,N)₃ with SrW(O,N)₃ to demonstrate the broader presence of such disorder and identify contrasting features in the electronic structures. This work signifies an updated perspective on the inherent crystal symmetry present in perovskite oxynitrides.

New concepts

We challenge the conventional reporting of crystal symmetry in perovskite oxynitrides through our exploration of the crystal structure of CaW(O,N)₃, which we synthesize for the first time. Traditional literature simplifies perovskite oxynitrides by using high-symmetry unit cells with fractional anion occupancy (*e.g.*, sites comprised of 50% O and 50% N). While these models provide a convenient approximation, they can never accurately reflect the true nature of perovskite oxynitrides. The reality is more complex; each anion site must contain either O or N, resulting in local displacements of the anions and neighboring cations off of their high-symmetry sites due to the differing ionic radii of O^{2-} and N^{3-}. We demonstrate using Rietveld co-refinement that a large unit cell (≥ 20 atoms) with low symmetry (space group $P1$) and random but defined anion positions provides a more accurate fit to the X-ray and neutron diffraction patterns for CaW(O,N)₃, affording unique insight into sources of disorder that are not captured within the traditional models. We find the same result for previously-reported SrW(O,N)₃, indicating that this disorder is more widespread than previously realized. Thus, this work presents a new perspective on the symmetry of perovskite oxynitrides and the crystal structures we use to describe them.

1. Introduction

For many electrochemical reaction systems, the lack of sufficiently active, durable, and affordable catalysts necessitates continued materials discovery and characterization. Heteroanionic materials, a relatively understudied class of inorganic materials that contain more than one type of anion species, have been demonstrated as attractive options for energy and electrochemistry applications owing to their highly tunable structures, compositions, and properties. For example, oxysulfides (materials containing both oxide and sulfide anions) exhibit high activity for oxygen evolution, oxygen reduction, and hydrogen evolution,[1–6] including in zinc–air batteries where increased activity is attributed to sulfur-tuned Co–O covalency.[7] Oxyfluorides have been demonstrated as catalysts for CO_2 reduction[8] and ethane oxidation[9] as well as solid oxide electrolytes for fuel cells.[10,11]

Oxynitrides, and notably perovskite oxynitrides which follow the formula AB(O,N)₃, are often studied as photocatalysts[12–18] and non-toxic pigments[19,20] due to their tendency for visible-range band gaps. Oxynitrides are typically synthesized *via* ammonolysis, whereby an oxide precursor is heated under flowing ammonia to incorporate nitrogen into the material.[21] The introduction of nitrogen into an oxide material can increase the covalency of the metal-anion bonds and form cations in heightened oxidation states due to nitrogen's

[a] *Department of Materials Science and Engineering, Northwestern University, Evanston, IL 60208, USA*

[b] *Department of Chemical and Biological Engineering, Northwestern University, Evanston, IL 60208, USA. E-mail: linsey.seitz@northwestern.edu*

[c] *Advanced Photon Source, Argonne National Laboratory, Lemont, IL 60439, USA*

[d] *Department of Physics and Astrophysics, DePaul University, Chicago, IL 60614, USA*
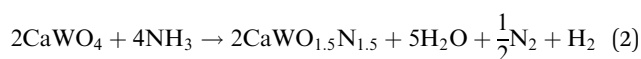
decreased electronegativity and more negative formal charge. Beyond electronic changes, oxynitrides can take on entirely new structures from their oxide counterparts,[22] unlocking new phase spaces that are inaccessible for some mixed-metal oxides. In perovskites, these phases tend to exhibit non-cubic symmetries due to distortion of the BX_6 octahedra, and in some cases, ordered arrangements of anions[23–26] not allowed within cubic space groups. Though slight atomic displacements of cations from high symmetry positions have been discussed,[25,26] the structures reported for perovskite oxynitrides are broadly described without these displacements in mind, leading to an incomplete structural picture.

In this work, we describe the first reported synthesis of calcium tungsten oxynitride $CaW(O,N)_3$, a perovskite oxynitride that is previously only predicted computationally, and use X-ray and neutron diffraction to investigate its crystal structure. We use Rietveld refinement complemented with density functional theory (DFT) calculations to examine its crystal structure, including octahedral distortion, anion ordering, and symmetry. Comparisons among different structural models help to identify sources of disorder, particularly from varying coordination environments. Further comparison with an analogous material, $SrW(O,N)_3$, supports these findings and highlights variations in electronic structure.

2. Results and discussion

Following the first step of a solid state reaction of calcium carbonate and tungsten(VI) oxide *via* grinding and calcining at 1000 °C for 4 h (Fig. 1a, details in Methods section), X-ray diffraction (XRD) confirms phase purity of the $CaWO_4$ scheelite intermediate (Fig. 1b) with minor additional peaks caused by Cu Kβ radiation. As expected, $CaWO_4$ peaks occur at larger angles compared with its $SrWO_4$ analogue due to the smaller ionic radius of Ca compared with Sr[27] (Fig. S1, ESI†). The oxynitride phases $CaW(O,N)_3$ and $SrW(O,N)_3$ were formed *via* ammonolysis at 700 °C for 12 h, and 900 °C for 5 h, respectively. We note that the ammonolysis temperature of 700 °C for $CaW(O,N)_3$ is lower than previously reported attempts to synthesize this material.[22,28] The proposed overall reaction follows as provided in eqn (1) and (2) below:

$$WO_3 + CaCO_3 \rightarrow CaWO_4 + CO_2 \quad (1)$$

$$2CaWO_4 + 4NH_3 \rightarrow 2CaWO_{1.5}N_{1.5} + 5H_2O + \frac{1}{2}N_2 + H_2 \quad (2)$$

Surface composition is estimated using X-ray photoelectron spectroscopy, which also confirms the lack of contaminants (Fig. S2 and Table S1, ESI†). We measured anion stoichiometry using combustion analysis, finding an overall composition of $CaWO_{3-x}N_x$ where $1.3 \leq x \leq 1.6$ (Table S2 (ESI†), details in Methods section). It is notable that this range captures the 1 : 1 anion ratio, which could potentially allow the structure to adopt an ordered configuration of anions.
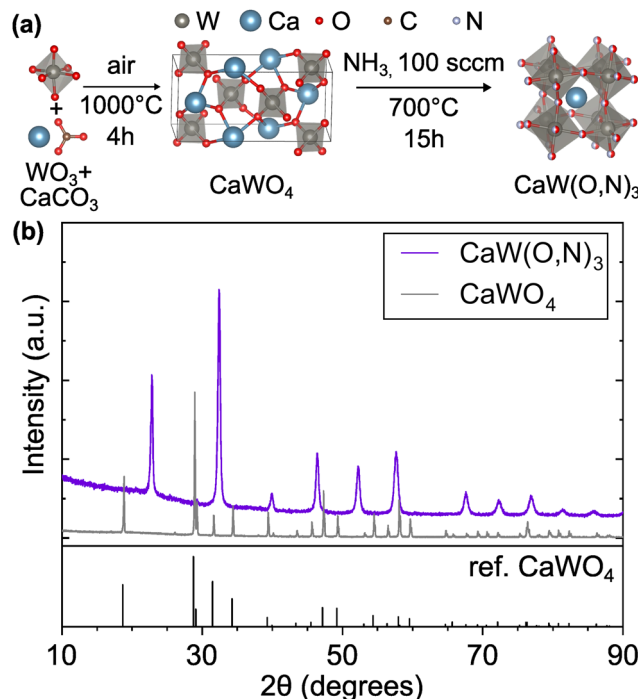

Fig. 1 (a) Synthesis route for $CaW(O,N)_3$ consisting of calcination of WO_3 and $CaCO_3$ precursors followed by ammonolysis of the scheelite $CaWO_4$ intermediate. (b) XRD patterns of intermediate scheelite phases, $CaWO_4$ and $CaW(O,N)_3$, demonstrating their differing crystal structures. $CaWO_4$ reference is provided.[29] Crystal structure images generated using VESTA.[30]

We performed Rietveld refinement[31] on synchrotron XRD and neutron diffraction (ND) patterns of $CaW(O,N)_3$ using several structural models (Table 1) to characterize its crystal structure. The tolerance factor for this material was calculated from Shannon radii,[27] accounting for varied W oxidation states. The calculated tolerance factor ranges between 0.923 for $CaWO_3$, which is not a stable material but represents the "oxide" extreme of the composition range, and 0.964 for $CaWON_2$,[32] where the oxidation state of W is maximized at 6+. Based on this range, one may expect this material to exhibit cubic symmetry regardless of anion stoichiometry,[33–36] though the tolerance factor is more commonly used for simple stability prediction.

Indeed, the XRD pattern for $CaW(O,N)_3$ displays a peak footprint matching a $Pm\bar{3}m$ space group (Fig. S3, ESI†), which is reported for $SrW(O,N)_3$,[22] though we observe minor additional peaks from the oxide $CaWO_4$ that formed in the capillary tube during transit time between sample submission and measurement as well as mismatches between the experimental and simulated peak intensities at low Q values. Furthermore, comparison of the ND pattern with the $Pm\bar{3}m$ model (C-I, Fig. S3b, ESI†) reveals numerous additional peaks that are not accounted for by $CaWO_4$, particularly evident in the $Q \approx 2 - 10$ Å^{-1} ($d \approx 3.1 - 0.6$ Å) region. The X-ray diffraction signal is dominated by heavy elements, whereas ND is more sensitive to light atoms such as O and N. As such, the fact that extra peaks are much less apparent in XRD (see Fig. S4, ESI†) but readily observed *via* ND indicates the presence of octahedral

Table 1 Structural models used for Rietveld refinement of CaW(O,N)₃ XRD and ND data. DFT IDs correspond to structures also described in Table 3. Model C-X uses anisotropic thermal parameters

Model	DFT ID	Space group	Atoms/unit cell	(O,N)₃ stoichiometry	Anion disorder method	Anion site occupancy
C-I	—	$Pm\bar{3}m$	5	$O_{1.5}N_{1.5}$	Partial occupancy	Fixed
C-II	—	$Pnma$	20	$O_{1.5}N_{1.5}$	Partial occupancy	Varied
C-III	—	$Pnma$	20	$O_{1.5}N_{1.5}$	Partial occupancy	Fixed
C-IV	—	$Pnma$	20	$O_{1.4}N_{1.6}$	Partial occupancy	Varied
C-V	—	$Pnma$	20	$O_{1.7}N_{1.3}$	Partial occupancy	Varied
C-VI	—	$Pnma$	20	O_3	Partial occupancy	Fixed
C-VII	—	$Pnma$	20	N_3	Partial occupancy	Fixed
C-VIII	F	$P1$	20	$O_{1.5}N_{1.5}$	Quasi-random	Fixed
C-IX	A	$P1$	60	$O_{1.5}N_{1.5}$	Quasi-random	Fixed
C-X	—	$Pnma$	20	$O_{1.5}N_{1.5}$	Partial occupancy	Varied

distortion that forms planes of O and N atoms with new inter-planar spacing while leaving Ca and W species relatively unmoved from their atomic planes.

We find that the ND peak positions and intensities are much more closely matched by an orthorhombic perovskite structure with space group $Pnma$ (model C-II, Fig. 2 and Fig. S5, ESI† and
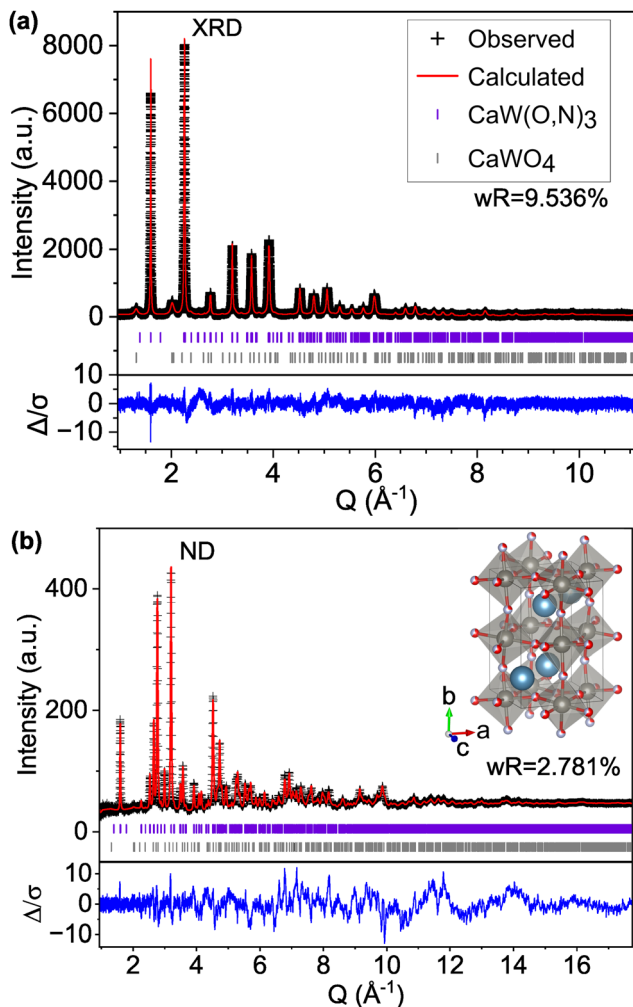

Fig. 2 Rietveld refinement of CaW(O,N)₃ (a) synchrotron XRD and (b) ND patterns to structural model C-II with the $Pnma$ space group and anion sites fractionally occupied by O and N.

Table 2), which is widely reported[37] for other perovskite oxynitrides and contains distorted octahedra. This structural change results in a significant reduction in the ND weighted residual (wR) from 12.514% for C-I ($Pm\bar{3}m$) to 2.763% for C-II ($Pnma$) and does better to match very minor peaks in the XRD pattern that were unmatched by the cubic C-I model (Fig. S4, ESI†). Additionally, we find from refinement results using the $Pnma$ structure (C-II) that N species may prefer the apical O1/N1 anion site over the O2/N2 site located in-plane with W atoms, accounting for 71% of the atoms on the O1/N1 site (Table 2 and Fig. S6, ESI†). Similar results have been found for other perovskite oxynitrides,[38,39] though the preference for nitrogen to occupy the apical site is somewhat unexpected in the broader context of the literature,[40,41] as it suggests that the anions prefer *trans* and *mer* configurations (see Fig. S7, ESI†). *Trans* configurations are generally regarded as less stable than *cis* ordering,[23,24,26,42] and *mer* configurations would result in N–W–N chains that would induce localized strain due to mismatched ionic radii and result in relative instability.[42] Both models contain 1 : 1 anion stoichiometry, but whereas model C-II allows O and N site occupancies to vary between sites O1/N1 and O2/N2, model C-III fixes the occupancies at 0.5 for both O and N on both anion sites. The refinement of site occupancy in C-II offers minor improvements in overall wR (from 5.041% for fixed to 4.993% for varied) and ND wR (from 2.817% for fixed to 2.763% for varied, Table S3, ESI†). Since refinement of site occupancy introduces additional degrees of freedom, we use the F-test to determine whether the observed improvement is statistically significant.[43,44] Based on the number of refined parameters for both refinements and total number of observations, an F ratio of ≥ 2.605 would signify a ≥ 0.95 probability of significance. From the weighted sums of squared residuals, we calculate an F ratio of 636.3. Thus, we conclude that there is sufficient evidence for preferred anion occupancy in model C-II. This preferential occupancy of N onto one type of anion site may influence the materials' optical and electronic properties, such as its dielectric constant.[23,26,45,46]

We also varied the global anion stoichiometry of the $Pnma$ model (C-II) used in Fig. 2 and Table 2 Table S3 (ESI†) to the extremities of the anion range estimated from combustion analysis (Table S2, ESI†) to test its impact on the fit. The resulting wR values for CaWO₁.₄N₁.₆ (model C-IV) and CaWO₁.₇N₁.₃ (model C-V) reported in Table 3 show no significant

Table 2 Structural parameters for CaW(O,N)$_3$ from Rietveld refinement of diffraction patterns with the GdFeO$_3$ perovskite structural prototype (model C-II)

Formula	CaWO$_{1.5}$N$_{1.5}$
Formula weight	262.929 Da
Formula units per unit cell (Z)	4
S.G. #	62
S.G.	Pnma
Crystal system	Orthorhombic
a	5.5708(1) Å
b	7.8598(2) Å
c	5.5326(1) Å
Volume	242.245(5) Å^3

Site	x	y	z	Occ.	Uiso
Ca	0.5174(4)	0.25	0.5023(7)	1	0.0170(2)
W	0.5	0	0	1	0.01737(7)
O1	0.4895(3)	0.25	0.0597(2)	0.29(1)	0.0120(2)
N1	—	—	—	0.71(1)	—
O2	0.2887(1)	0.0302(1)	0.7106(2)	0.607(5)	0.0068(1)
N2	—	—	—	0.393(5)	—

improvement in the fit with varied anion ratio compared with CaWO$_{1.5}$N$_{1.5}$ (model C-II). We further examined the impact of anion stoichiometry on predicted ND patterns by extending the model composition to CaWO$_3$ (model C-VI) and CaWN$_3$ (model C-VII) in Fig. S8 (ESI†). Peaks at $Q \approx 3.20$, 2.77, and 2.26 Å^{-1} (d = 1.96, 2.27, 2.78) exhibit the greatest sensitivity to anion stoichiometry. However, while the observed pattern falls between the all-O and all-N signals, the proportions of mismatch between each model and the observed data are not consistent across peaks, suggesting that the variation in ND peak intensities cannot be accounted for by anion stoichiometry alone.

While the Pnma structure from model C-II above provides an excellent match to the ND signal, the significant mismatch between the observed and modeled pseudocubic (001) peak intensity (≈ 1.6 Å^{-1} in the XRD pattern) indicates there is disorder that is not fully captured by the strictly defined atomic positions and symmetry. To identify additional structure candidates and further investigate anion ordering in CaW(O,N)$_3$, we complemented our experimental approach and literature-sourced model crystal structures with structures provided by DFT calculations. We calculated the stability (defined as energy above the convex hull, E_{hull}, containing 0.5 mol CaO + 0.167 mol Ca$_3$WO$_6$ + 0.25 mol N + 0.417 mol W$_2$N$_3$ according to the Open Quantum Materials Database, OQMD) for structures with both ordered and disordered anion configurations and parent cells representing multiple space groups, summarized in Table 4. Notably, nearly all structures that are predicted

Table 3 Weighted residuals from Rietveld refinement of orthorhombic Pnma structural models for CaW(O,N)$_3$ with varied anion stoichiometries representing possible compositions

Model	(O,N)$_3$ stoichiometry	wR (%)	XRD wR (%)	ND wR (%)
C-IV	O$_{1.4}$N$_{1.6}$	5.046	9.544	2.813
C-II	O$_{1.5}$N$_{1.5}$	5.029	9.536	2.781
C-V	O$_{1.7}$N$_{1.3}$	5.004	9.524	2.736

to be relatively low in energy ($E_{hull} < 50$ meV atom^{-1} [47,48]) exhibit disordered anion configurations. We used these low energy structures for Rietveld refinement with the experimental data.

For comparison with the Pnma structure (model C-II) which contains 20 atoms per unit cell, we first examine the low energy structures in Table 4 with at most 20 atoms per unit cell. Of this subset, model Structure F (model C-VIII) with $P1$ symmetry and defined anion positions provides the best fit to the experimental data (Fig. S9, ESI†), exhibiting improvement over the Pnma structure for both XRD (improving wR from 9.536% for C-II to 8.758% for C-VIII) and ND (improving ND wR from 2.781% for C-II to 2.653% for C-VIII). Notably, model C-VIII exhibits a significantly improved match to the pseudocubic (001) XRD peak intensity at $Q \approx 1.6$ Å^{-1} compared with model C-II, though there are peaks present in the low Q region of the modeled ND pattern, particularly at 1.13 and 2.78 Å^{-1}, that are not supported by the experimental data. By contrast, the lowest energy predicted structure (structure A, model C-IX) with the same $P1$ symmetry and a larger 60-atom cell provides an excellent match to both the XRD and ND patterns (Fig. 3), achieving the lowest wR values for both the XRD and ND patterns of any structure tested (structural details are provided in Tables S4 and Table S5 and Fig. S10, ESI†). Nevertheless, there are still features in the modeled ND pattern that are not present in the observed data, though these discrepancies are smaller than those apparent for smaller unit cells and approaching the order of magnitude of the background noise.

It is important to note that such improvement over the more constrained C-II model is expected given the large increase in the number of refined parameters between the models (47 parameters for C-II and 224 parameters for C-IX). Thus, we do not identify model C-IX containing P1 symmetry as the true structure of CaW(O,N); rather, we use this model to discuss sources of disorder in the material. For example, in model C-II where fractional site occupancy is used to model anion disorder, the position of the anion sites, the bond lengths, and the positions of neighboring cations all remain invariant to the identity of the anion in order to maintain symmetry. Even when we simulate additional disorder in the Pnma model through the refinement of anisotropic thermal parameters, which results in an improvement to total wR (from 4.993% for model C-II to 4.797% for model C-X), the Pnma models still only describe the long-range average crystal structure; they do not accurately represent the local distortions to Ca and W sites that physically occur in this material as a result of their varied anion coordinations.

Disordered anion configurations leave each W atom with numerous possible permutations of the WX$_6$ octahedral environment that place W in various oxidation states and impose different perturbations to the atomic positions due to the difference in the ionic radii of O^{2-} (1.4 Å) and N^{3-} (1.64 Å).[27] Such perturbations cannot be fully represented by a highly symmetric unit cell and would decrease the intensity of XRD peaks, which are highly sensitive to the cation symmetry due to their larger atomic numbers in this material. We propose that these

Table 4 Summary of DFT-calculated ordered structures for CaW(O,N)$_3$ with O$_{1.5}$N$_{1.5}$ anion stoichiometry, where structures with convex hull distance <0.05 eV atom^{-1} (above the horizontal line) are low energy and used for Rietveld refinement with the experimental data. "–" denotes a disordered anion configuration

DFT ID	Composition	S.G. #	Crystal system	Spage group	Anion ordering	# of atoms	E_{hull} (eV atom^{-1})
A	CaWO$_{1.5}$N$_{1.5}$	1	Triclinic	$P1$	—	60	0.026
B	CaWO$_{1.5}$N$_{1.5}$	1	Triclinic	$P1$	—	40	0.034
C	CaWO$_{1.5}$N$_{1.5}$	1	Triclinic	$P1$	—	40	0.034
D	CaWO$_{1.5}$N$_{1.5}$	1	Triclinic	$P1$	—	20	0.035
E	CaWO$_{1.5}$N$_{1.5}$	1	Triclinic	$P1$	—	20	0.037
F	CaWO$_{1.5}$N$_{1.5}$	1	Triclinic	$P1$	—	20	0.037
G	CaWO$_{1.5}$N$_{1.5}$	1	Triclinic	$P1$	—	20	0.038
H	CaWO$_{1.5}$N$_{1.5}$	1	Triclinic	$P1$	—	20	0.039
I	CaWO$_{1.5}$N$_{1.5}$	1	Triclinic	$P1$	—	20	0.042
J	CaWO$_{1.5}$N$_{1.5}$	1	Triclinic	$P1$	—	40	0.043
K	CaWO$_{1.5}$N$_{1.5}$	1	Triclinic	$P1$	—	40	0.047
L	CaWO$_{1.5}$N$_{1.5}$	166	Trigonal	$R\bar{3}m$	Fac	10	0.049
M	CaWO$_{1.5}$N$_{1.5}$	1	Triclinic	$P1$	—	160	0.061
N	CaWO$_{1.5}$N$_{1.5}$	1	Triclinic	$P1$	—	20	0.068
O	CaWO$_{1.5}$N$_{1.5}$	1	Triclinic	$P1$	—	20	0.071
P	CaWO$_{1.5}$N$_{1.5}$	1	Triclinic	$P1$	—	40	0.071
Q	CaWO$_{1.5}$N$_{1.5}$	25	Orthorhombic	$Pmm2$	Cis	10	0.076
R	CaWO$_{1.5}$N$_{1.5}$	1	Triclinic	$P1$	—	20	0.078
S	CaWO$_{1.5}$N$_{1.5}$	1	Triclinic	$P1$	—	20	0.08
T	CaWO$_{1.5}$N$_{1.5}$	115	Tetragonal	$P\bar{4}m2$	Mer	10	0.107
U	CaWO$_{1.5}$N$_{1.5}$	65	Orthorhombic	$Cmmm$	Mer	10	0.111
V	CaWO$_{1.5}$N$_{1.5}$	69	Orthorhombic	$Fmmm$	Mer	10	0.113
W	CaWO$_{1.5}$N$_{1.5}$	99	Tetragonal	$P4mm$	Segregated octahedra	10	0.117
X	CaWO$_{1.5}$N$_{1.5}$	65	Orthorhombic	$Cmmm$	Mer	10	0.119
Y	CaWO$_{1.5}$N$_{1.5}$	47	Orthorhombic	$Pmmm$	Mer	10	0.121
Z	CaWO$_{1.5}$N$_{1.5}$	47	Orthorhombic	$Pmmm$	$Trans$	10	0.142
AA	CaWO$_{1.5}$N$_{1.5}$	65	Orthorhombic	$Cmmm$	$Trans$	10	0.144
AB	CaWO$_{1.5}$N$_{1.5}$	47	Orthorhombic	$Pmmm$	$Trans$	10	0.147

perturbations have a far weaker effect on the predicted ND pattern for CaW(O,N)$_3$ due to the fact that in the *Pnma* model (C-II), the anions are already displaced from high-symmetry sites due to octahedral rotation, so further displacement does not have as great an effect on the site symmetry of anions. This concept of varied local coordinations, called disproportionation, hints at the broader dichotomy prevalent within discussion of defective and non-stoichiometric materials of whether to describe materials by their local or periodic structures.[49–53] Disproportionation leads to a high-symmetry average structure with lower local symmetry referred to as a "polymorphous network".[50,54–56] Polymorphism is also found in oxide and halide perovskites and is linked with band narrowing, metal-to-insulator transitions, and the formation of unique hole states.[56]

While a material with truly random anion placement would theoretically contain 4 : 1 and 2 : 3 ratios of *cis* : *trans* and *fac* : *mer* anion configurations (refer to Fig. S7, ESI†), respectively, the literature and our own theory-based work suggest that octahedra with *cis* and *fac*-type anion configurations would be more prevalent than those with *trans* and *mer* configurations based on energetic arguments.[23,24,26,40,42,57] Indeed, in our lowest-energy predicted "anion disordered" structures, the majority of the octahedral configurations are *cis*-type, but not repeated in a consistent or symmetric manner. Accordingly, large unit cell size is necessary to sufficiently approximate the lack of consistently repeating anion motifs and a range of atomic displacements while maintaining a high fraction of WX$_6$ octahedra with *cis*-type anion configurations.

When we apply this understanding of atomic position perturbations resulting from varied coordination environments in heteroanionic materials to the previously reported[22,28,58] perovskite oxynitride SrW(O,N)$_3$, we find similar improvements of the fit with the experimental data. We first apply the reported structure model for this material, a cubic structure with the space group $Pm\bar{3}m$ and disordered anions (model S-I, Table 5), to the experimental data and find good agreement between peak positions in both the XRD and ND patterns, but poorly matched peak intensities as revealed by the sharp features in the Δ/σ plots (Fig. S11, ESI†). Additional structural details are reported in Table S6 (ESI†).

However, if we apply the concepts from model C-IX and use an anion-disordered $P1$ structure with a 40-atom unit cell (model S-II) that breaks the global symmetry and allows for displacement of all atomic positions, we are able to more accurately match peak intensities (Fig. 4). This results in improved fits compared with the $Pm\bar{3}m$ structure for both the XRD pattern (16.085% wR for S-I down to 12.649% for S-II) and ND pattern (5.707% wR for S-II down to 4.431% for S-II). Hints of atomic displacement in SrW(O,N)$_3$ were presented in a previous study of its extended X-ray absorption fine structure (EXAFS), where it was reported that the nearest neighbor scattering interaction required more than one W-anion scattering path to achieve a reasonable fit,[58] as would be required for a W atom displaced from the center of its coordination octahedron. Curiously, while model S-II results in decreased residuals compared with model S-I (see Fig. 4 and Fig. S11, ESI†),
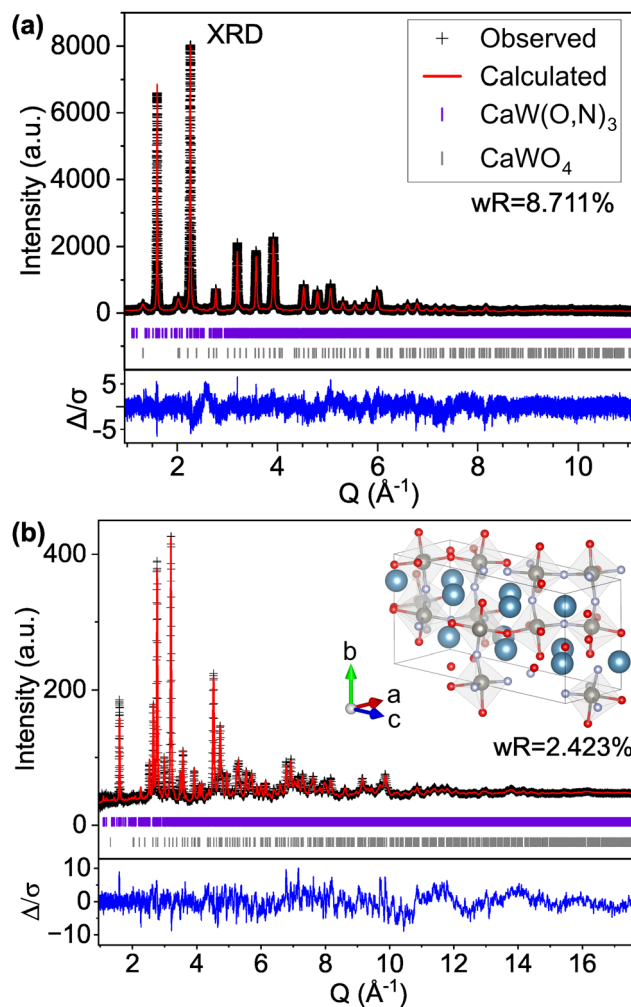
Fig. 3 Rietveld refinement of $CaW(O,N)_3$ (a) synchrotron XRD and (b) ND patterns to the most stable DFT-determined structure that contains $P1$ symmetry and disordered anions (model C-IX, structure A) and provides the best fit to the experimental data.

Fig. 4 Rietveld refinement of $SrW(O,N)_3$ (a) synchrotron XRD and (b) ND patterns using a 40-atom $P1$ structure suggested by our theory-based approaches (model S-II).

there still exists clear systematic error in the peak fits, which may suggest further sources of disorder not accounted for by the P1 model.[59] Similar to our findings for $CaW(O,N)_3$, this structure still results in minor peaks in the high d (low Q) region of the calculated pattern that are on the order of magnitude of background noise. Additional structural details are provided in Tables S7 and S8 (ESI†). Based on the evidence presented in this work for both $CaW(O,N)_3$ and $SrW(O,N)_3$, we assert that disproportionation and polymorphism may be more widely present within perovskite oxynitrides (and potentially the broader category of oxynitrides) and should be addressed when discussing their crystal structures.
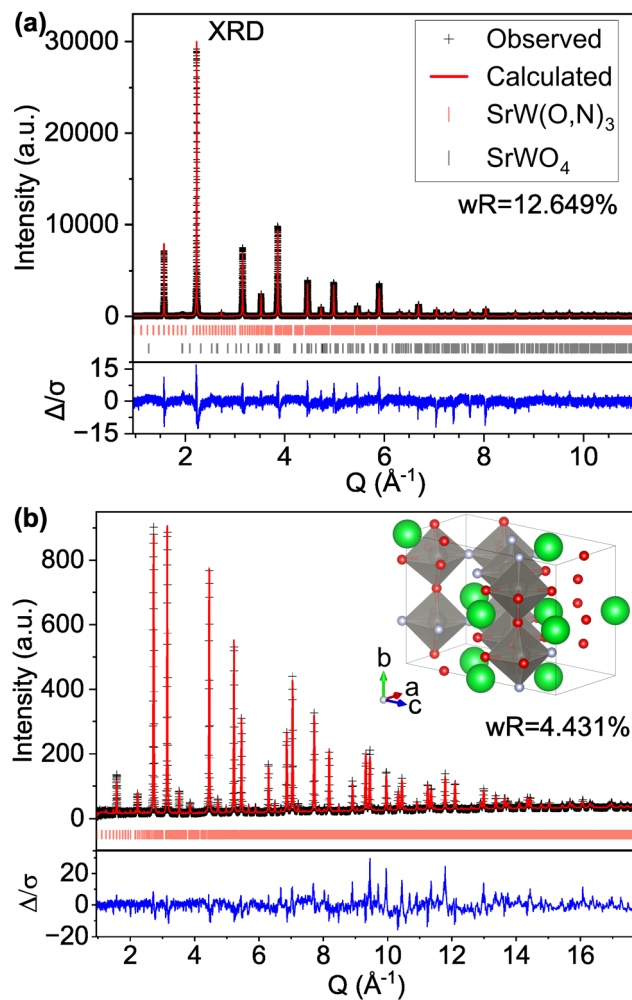
To investigate electronic structure differences between $CaW(O,N)_3$ and its analogue $SrW(O,N)_3$, we performed X-ray absorption spectroscopy (XAS) measurements at the O and N K-edges. For the O K-edge (Fig. 5a), the first features in the spectra occur at ∼532.2 eV and are attributed to electron transitions from O 1s states to O 2p – W 5d t_{2g} hybridized states.[60] The features in the region 533.5–538 eV are typically attributed to electron transitions from O 1s states to O 2p – W 5d e_g hybridized states in tungstates,[60,61] though for complex oxides, the absorption can be influenced by covalent interactions with the A-site species.[61] Yashima $et\ al.$ calculated via DFT the partial density of states for the $Ca_xSr_{1-x}WO_2N$

Table 5 Structural models used for Rietveld refinement of $SrW(O,N)_3$ XRD and ND data

Model	Space group	Atoms/unit cell	$(O,N)_3$ stoichiometry	Anion disorder method	Anion site occupancy
S-I	$Pm\bar{3}m$	5	$O_{1.5}N_{1.5}$	Partial occupancy	Fixed
S-II	$P1$	40	$O_{1.5}N_{1.5}$	Randomized	Fixed

composition system, from which we observe that the unoccupied Ca 3d states are expected to exist at lower energies than the Sr 4d states.[22] Although the composition range calculated in that work does not extend all the way to $CaWO_2N$, the relative energies of Ca 3d and Sr 4d states appear to align with the observed features in our XAS data. Namely, $CaW(O,N)_3$ exhibits greater absorption intensity approximately 4 eV above the absorption edge (at $\sim$534 eV), whereas $SrW(O,N)_3$ shows greater absorption intensity >5 eV above the absorption edge (at >535 eV). Since both materials are metallic, the Fermi energy should approximately align with the observed absorption edges.

For an electrically conductive material in which the O and N anions occupy the same lattice sites, we can reasonably expect O and N 2p states to hybridize with the same unoccupied electronic states above the Fermi level. This expectation is largely confirmed by the N K-edge spectra (Fig. 5b), which reflect very similar features to the O K-edge spectra. At both edges, we observe that the intensities of the anion 2p – W 5d t_{2g} features (532.2 eV for O K and 398 eV for N K) are greater for $SrW(O,N)_3$ than for $CaW(O,N)_3$. This disparity suggests increased covalency between anions and 5d t_{2g} states in $SrW(O,N)_3$ compared with $CaW(O,N)_3$, which contrasts with previously reported results regarding the effect of Sr vs. Ca on covalency in a perovskite.[62] At higher energies in the N K-edge spectra, we observe the same trend in relative intensity as seen at the O K-edge, which we propose are attributed to the disparate energies of the Ca 3d and Sr 4d states. The sharp feature at 401.5 eV is likely a result of diffraction due to the large unit cell and is not representative of true electronic states, as it is not observed in the total electron yield (TEY) signals (Fig. S12, ESI†). Since the greatest differences in the XAS signal for $CaW(O,N)_3$ and $SrW(O,N)_3$ are likely a result of varied Ca and Sr d-state energies, the impact of octahedral distortion on the electronic structure is not readily observed from these spectra. However, these results provide sufficient evidence to demonstrate octahedral distortion and the existence of additional disorder in $CaW(O,N)_3$ that may be present, yet have been previously underrecognized in a broader array of oxynitride materials.

3. Methods

3.1. Materials synthesis

Calcium carbonate ($CaCO_3$, Sigma-Aldrich, $\geq$99%) and tungsten(VI) oxide (WO_3, Sigma-Aldrich, 99.9%) were ground together in a stoichiometric metals ratio with a mortar and pestle, heated in an alumina crucible at 1000 °C for 4 h, and allowed to cool naturally to form $CaWO_4$. This material was ground in a mortar and pestle for 30 min. To form $SrWO_4$, the same procedure was followed using strontium carbonate ($SrCO_3$, Aldrich, 99.995%) and heating to 900 °C for 12 h. Both powders appear white in color.

To form $CaW(O,N)_3$, 500 mg of the $CaWO_4$ intermediate was loaded into a quartz boat and placed in a fused quartz tube in a tube furnace. Anhydrous ammonia was flowed through the tube at 100 sccm. The sample was heated at 3.3 °C min^{-1} to 700 °C and held for 15 h. The same procedure was used to form $SrW(O,N)_3$ by placing $SrWO_4$ in the quartz boat and heating to 900 °C for 5 h. The resulting powders are dark gray in color.

3.2. Combustion analysis

We used combustion analysis (Midwest Microlabs) to measure the nitrogen content in the material (Table S2, ESI†), which we use to estimate stoichiometry assuming a 1:1 cation ratio and negligible anion vacancy concentration. Using the H wt% values, we corrected the nitrogen weight fraction to account for adsorbed ammonia species. The range of anion stoichiometry in $CaWO_{3-x}N_x$ we report in Table S2 (ESI†), $1.3 \leq x \leq$
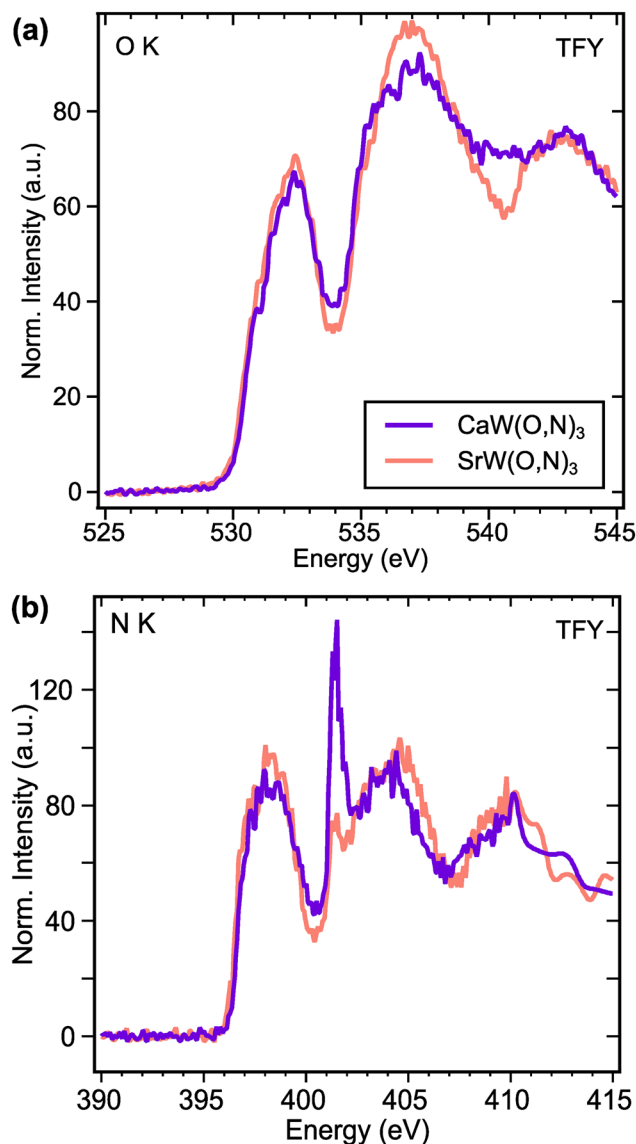

Fig. 5 (a) Oxygen and (b) nitrogen K-edge XAS spectra of $CaWO_2N$ and $SrWO_2N$ perovskite powder samples measured in total fluorescence yield. Intensities are area-normalized between 528–545 eV for O K-edge and 394–410 eV for N K-edge.

1.6, is relatively wide due to uncertainty in the hydrogen and nitrogen weight fractions.

3.3. Lab X-ray diffraction

For determining the structure and purity of the scheelite intermediates, we collected powder X-ray diffractograms using a Rigaku Smartlab system equipped with a Cu rotating anode using Cu Kα radiation (wavelength = 1.5418 Å). The accelerating voltage between the W filament and the anode was set at 40 kV and the tube current was 35 mA. Data were collected using a Hypix area detector. Samples were ground with a mortar and pestle before measurement.

3.4. Synchrotron X-ray diffraction

High resolution synchrotron powder diffraction data were collected using the mail-in program for beamline 11-BM at the Advanced Photon Source (APS), Argonne National Laboratory using an average wavelength of 0.45904 Å. Discrete detectors covering an angular range from −6 to 16° 2θ are scanned over a 34° 2θ range, with data points collected every 0.001° 2θ and scan speed of 0.01° per s.

The 11-BM instrument uses X-ray optics with two platinum-striped mirrors and a double-crystal Si(111) monochromator, where the second crystal has an adjustable sagittal bend.[63] Ion chambers monitor incident flux. A vertical Huber 480 goniometer, equipped with a Heidenhain encoder, positions an analyzer system comprised of twelve perfect Si(111) analyzers and twelve Oxford-Danfysik LaCl$_3$ scintillators, with a spacing of 2° 2θ.[64] Analyzer orientation can be adjusted individually on two axes. A three-axis translation stage holds the sample mounting and allows it to be spun, typically at ~5400 rpm (90 Hz). A Mitsubishi robotic arm is used to mount and dismount samples on the diffractometer. An Oxford Cryosystems Cryostream Plus device allows sample temperatures to be controlled over the range 80–500 K when the robot is used. Samples were measured at 298 K.

The diffractometer is controlled via EPICS.[65] Data are collected while continually scanning the diffractometer 2θ arm. A mixture of NIST standard reference materials, Si (SRM 640c) and Al$_2$O$_3$ (SRM 676) is used to calibrate the instrument, where the Si lattice constant determines the wavelength for each detector. Corrections are applied for detector sensitivity, 2θ offset, small differences in wavelength between detectors, and the source intensity, as noted by the ion chamber before merging the data into a single set of intensities evenly spaced in 2θ.

3.5. Neutron diffraction

We collected neutron diffraction patterns using the mail-in program for the POWGEN instrument at Oak Ridge National Laboratory's Spallation Neutron Source. Approximately 3 g of each measured powder were loaded into vanadium cans for shipment and measurement. We used data from Neutron Bank 1 scanned over the time of flight (TOF) range of 3617 to 176 000 μs (d-spacing of 0.354 to 6.65 Å) measured at ambient temperature.

3.6. Combined refinement approach

We carried out Rietveld refinements of X-ray and neutron diffraction patterns using GSAS-II software.[66] XRD and ND patterns were weighted equally during refinement. We used Inverse Chebyshev polynomials to accurately follow the curvature of the background for both diffraction patterns. For XRD, we assigned limits of $4.0° < 2\theta < 48.7°$ to exclude regions with no peaks and/or excessively noisy background signal. Sample X displacement (perpendicular to the beam) was allowed to vary. For ND, we assigned limits of 8000 μs < TOF < 150 000 μs to both (i) exclude highly noisy data at the extremities and (ii) include the 100 000–150 000 μs range where no peaks appeared in the data but several structural models displayed significant calculated peaks. Phase parameters were varied progressively in the following order: lattice parameter(s), crystallite size, microstrain, vibrational parameters (Uiso), site fraction, and atomic displacement (where possible). The scheelite oxide phases were added to CaW(O,N)$_3$ XRD, ND, and SrW(O,N)$_3$ XRD patterns and phase fractions were constrained to sum to 1. No oxide peaks were detected in the SrW(O,N)$_3$ ND pattern. For structures with anion disorder modeled via fractional anion occupancy, vibrational parameters for O and N were constrained to be equivalent since they occupy the same sites. For structures with large unit cells (>20 atoms), we constrained atomic fractions and vibrational parameters for all sites within each element type to be equivalent. For the XRD pattern, a total of 1177 peaks are identified when using the Pnma model, 725 belonging to CaW(O,N)$_3$ and 452 belonging to CaWO$_4$. For the ND pattern, a total of 4808 peaks are identified when using the Pnma model, 2958 belonging to CaW(O,N)$_3$ and 1850 belonging to CaWO$_4$.

3.7. Density functional theory calculations

Special quasirandom structures (SQS)[67] approximate random configurations employing a limited-size low-symmetry supercell. This cell is specifically chosen with cluster correlations that match as closely as possible the random values, particularly in the first few nearest neighbor shells, based on the assumption that short-range contributions to the energy typically have a stronger impact.[67,68] Consequently, the objective function to minimize for generating SQS is designed in the form of:[68]

$$Q = -\omega L + \sum_{\alpha} \left| \Gamma_{\alpha}^{SQS} - \Gamma_{\alpha}^{rnd} \right| \qquad (3)$$

where $\left| \Gamma_{\alpha}^{SQS} - \Gamma_{\alpha}^{rnd} \right|$ is the cluster correlation difference between a generated SQS and the perfect random limit, L is the length such that all clusters α with a diameter $< L$ satisfy $\left| \Gamma_{\alpha}^{SQS} - \Gamma_{\alpha}^{rnd} \right| = 0$, and ω is a customizable weight parameter to promote the perfect match in the first few shells. This study utilized the Pythonic ICET[69] package and Alloy Theoretic Automated Toolkit (ATAT)[70] to construct 40- and 60-atom anion-mixed SQS supercells derived from perovskite prototypes of varying symmetries. The structural relaxation and stability calculations were integrated in the Open Quantum Materials Database (OQMD)[71,72] framework, which employs the Vienna Ab initio Simulation Package (VASP)[73–75] with Projector

Augmented Wave (PAW)[76,77] potentials and the GGA-PBE[78] exchange–correlation.

3.8. X-ray absorption spectroscopy

The O and N K-edge absorption spectra of $CaW(O,N)_3$ and $SrW(O,N)_3$ were collected at beamline 29-ID-D of the Advanced Photon Source at Argonne National Laboratory. Absorption intensity was measured using total fluorescence yield and total electron yield. Each spectrum was processed for comparison by removing linear background in the pre-edge region, normalizing the integrated area in the edge region, and removing linear post-edge background.

4. Conclusions

We synthesized calcium tungsten oxynitride for the first time *via* ammonolysis and used combustion analysis to estimate its composition as $CaWO_{1.4-1.7}N_{1.3-1.6}$. Through comparison of Rietveld refinements of XRD and ND patterns with common perovskite structures, we identify the presence of octahedral distortion and evidence for preferred anion occupancy in this material, which may extenuate the anisotropy of materials properties already expected based on its orthorhombic *Pnma* average structure. Closer analysis of Rietveld refinements using DFT-predicted structures with various symmetry and anion ordering sheds light on additional disorder within the structure, which we propose stem from atomic displacements of both cations and anions resulting from varied ionic radii and configurations of nearest neighbors. Since such variations are inherent to anion-disordered materials, we postulate that these atomic displacements and polymorphism that modify electronic structure may be more prevalent than previously recognized in oxynitrides, which we also demonstrate with comparison to $SrW(O,N)_3$.

Author contributions

Matthew E Sweers was responsible for conceptualization, data curation, formal analysis, investigation, methodology, project administration, visualization, and writing of the original draft. Jiahong Shen and Tzu-chen Liu contributed investigation and methodology with DFT calculations. Bingzhang Lu performed investigation and methodology through material synthesis. John Freeland supported XAS measurements with methodology and formal analysis. Christopher Wolverton provided resources and guidance for DFT calculations. Gabriela B. Gonzalez Aviles contributed resources for ND beamtime and formal analysis of Rietveld refinements. Linsey C. Seitz was responsible for conceptualization, funding acquisition, resources, and supervision. All editors contributed to writing – review and editing.

Conflicts of interest

There are no conflicts to declare.

Acknowledgements

References

1 Y. Zhang, X. Wang, D. Hu, C. Xue, W. Wang, H. Yang, D. Li and T. Wu, *ACS Appl. Mater. Interfaces*, 2018, **10**, 13413–13424.

2 Z. Bai, S. Li, J. Fu, Q. Zhang, F. Chang, L. Yang, J. Lu and Z. Chen, *Nano Energy*, 2019, **58**, 680–686.

3 T. K.-C. Lê, Sorbonne Université, 2020.

4 S. Nandy, T. Hisatomi, M. Nakabayashi, H. Li, X. Wang, N. Shibata, T. Takata and K. Domen, *Joule*, 2023, **7**, 1641–1651.

5 G. Giuffredi, A. Mezzetti, A. Perego, P. Mazzolini, M. Prato, F. Fumagalli, Y.-C. Lin, C. Liu, I. N. Ivanov, A. Belianinov, M. Colombo, G. Divitini, C. Ducati, G. Duscher, A. A. Puretzky, D. B. Geohegan and F. Di Fonzo, *Small*, 2020, **16**, 2004047.

6 D. Ryaboshapka and P. Afanasiev, *J. Catal.*, 2023, **426**, 30–38.

7 J. Cai, H. Zhang, L. Zhang, Y. Xiong, T. Ouyang and Z.-Q. Liu, *Adv. Mater.*, 2023, **35**, 2303488.

8 Y. Li, Y. Li, Y. Wan, Y. Xie, J. Zhu, H. Pan, X. Zheng and C. Xia, *Adv. Energy Mater.*, 2019, **9**, 1803156.

9 H. X. Dai, C. F. Ng and C. T. Au, *J. Catal.*, 2000, **189**, 52–62.

10 F. Su, C. Xia and R. Peng, *J. Eur. Ceram. Soc.*, 2015, **35**, 3553–3558.

11 Z. Zhang, Y. Zhu, Y. Zhong, W. Zhou and Z. Shao, *Adv. Energy Mater.*, 2017, **7**, 1700242.

12 D. Pergolesi, C. Lawley and T. Lippert, *Sol. RRL*, 2022, **6**, 2200286.

13 A. Iborra-Torres, A. N. Kulak, R. G. Palgrave and G. Hyett, *ACS Appl. Mater. Interfaces*, 2020, **12**, 33603–33612.

14 K. Sawada and T. Nakajima, *APL Mater.*, 2018, **6**, 101103.

15 G. Lin, R. Wang, T. Cao, L. Yuan and X. Xu, *Inorg. Chem. Front.*, 2020, **7**, 2629–2636.

16 C. Pan, T. Takata, K. Kumamoto, S. S. Khine Ma, K. Ueda, T. Minegishi, M. Nakabayashi, T. Matsumoto, N. Shibata, Y. Ikuhara and K. Domen, *J. Mater. Chem. A*, 2016, **4**, 4544–4552.

17 M. Hojamberdiev, E. Zahedi, E. Nurlaela, K. Kawashima, K. Yubuta, M. Nakayama, H. Wagata, T. Minegishi, K. Domen and K. Teshima, *J. Mater. Chem. A*, 2016, **4**, 12807–12817.

18 S. Nishimae, Y. Mishima, H. Nishiyama, Y. Sasaki, M. Nakabayashi, Y. Inoue, M. Katayama and K. Domen, *Sol. RRL*, 2020, **4**, 1900542.

19 R. Aguiar, D. Logvinovich, A. Weidenkaff, A. Rachel, A. Reller and S. G. Ebbinghaus, *Dyes Pigm.*, 2008, **76**, 70–75.

20 F. Tessier, P. Maillard, F. Chevire, K. Domen and S. Kikkawa, *J. Ceram. Soc. Jpn.*, 2009, **117**, 1–5.

21 S. H. Elder, F. J. DiSalvo, L. Topor and A. Navrotsky, *Chem. Mater.*, 1993, **5**, 1545–1553.

22 M. Yashima, U. Fumi, H. Nakano, K. Omoto and J. R. Hester, *J. Phys. Chem. C*, 2013, **117**, 18529–18539.

23 M. Yang, J. Oró-Solé, J. A. Rodgers, A. B. Jorge, A. Fuertes and J. P. Attfield, *Nat. Chem.*, 2011, **3**, 47–52.

24 S. D. Young, J. Chen, W. Sun, B. R. Goldsmith and G. Pilania, *Chem. Mater.*, 2023, **35**, 5975–5987.

25 K. Page, M. W. Stoltzfus, Y.-I. Kim, T. Proffen, P. M. Woodward, A. K. Cheetham and R. Seshadri, *Chem. Mater.*, 2007, **19**, 4037–4042.

26 Y.-R. Zhang, T. Motohashi, Y. Masubuchi and S. Kikkawa, *J. Ceram. Soc. Jpn.*, 2011, **119**, 581–586.

27 R. D. Shannon, *Acta Crystallogr., Sect. A: Cryst. Phys., Diffr., Theor. Gen. Crystallogr.*, 1976, **32**, 751–767.

28 W. Li, D. Li, X. Gao, A. Gurlo, S. Zander, P. Jones, A. Navrotsky, Z. Shen, R. Riedel and E. Ionescu, *Dalton Trans.*, 2015, **44**, 8238–8246.

29 R. M. Hazen, L. W. Finger and J. W. E. Mariathasan, *J. Phys. Chem. Solids*, 1985, **46**, 253–263.

30 K. Momma and F. Izumi, *J. Appl. Crystallogr.*, 2011, **44**, 1272–1276.

31 H. Rietveld, *J. Appl. Crystallogr.*, 1969, **2**, 65–71.

32 V. M. Goldschmidt, *Naturwissenschaften*, 1926, **14**, 477–485.

33 C. J. Bartel, C. Sutton, B. R. Goldsmith, R. Ouyang, C. B. Musgrave, L. M. Ghiringhelli and M. Scheffler, *Sci. Adv.*, 2019, **5**, eaav0693.

34 W. Travis, E. N. K. Glover, H. Bronstein, D. O. Scanlon and R. G. Palgrave, *Chem. Sci.*, 2016, **7**, 4548–4556.

35 L. G. Chagas, J. L. F. Da Silva and M. P. Lima, *Phys. Rev. B*, 2024, **109**, 014106.

36 G. Wang, M. Lei, J. Liu, Q. He and W. Zhang, *Sol. RRL*, 2020, **4**, 2000528.

37 T. Wakasugi, Y. Hirose, S. Nakao, Y. Sugisawa, D. Sekiba and T. Hasegawa, *ACS Omega*, 2020, **5**, 13396–13402.

38 S. J. Clarke, K. A. Hardstone, C. W. Michie and M. J. Rosseinsky, *Chem. Mater.*, 2002, **14**, 2664–2669.

39 E. Günther, R. Hagenmayer and M. Jansen, *Z. Anorg. Allg. Chem.*, 2000, **626**, 1519–1525.

40 X. Xu and H. Jiang, *RSC Adv.*, 2020, **10**, 24410–24418.

41 N. Charles, R. J. Saballos and J. M. Rondinelli, *Chem. Mater.*, 2018, **30**, 3528–3537.

42 G. Pilania, A. Ghosh, S. T. Hartman, R. Mishra, C. R. Stanek and B. P. Uberuaga, *npj Comput. Mater.*, 2020, **6**, 71.

43 C. H. S. E. Prince, in *International Tables for Crystallography*, ed. E. Prince, 1st edn, 2006, vol. Volume C: Mathematical, physical and chemical tables, ch. 8. Refinement of Structural Parameters.

44 E. Prince, *Mathematical Techniques in Crystallography and Materials Science*, Springer Berlin Heidelberg, Berlin, Heidelberg, 2nd edn, 1994.

45 A. Fuertes, *Dalton Trans.*, 2010, **39**, 5942–5948.

46 M. Jansen and H. P. Letschert, *Nature*, 2000, **404**, 980–982.

47 W. Sun, S. T. Dacek, S. P. Ong, G. Hautier, A. Jain, W. D. Richards, A. C. Gamst, K. A. Persson and G. Ceder, *Sci. Adv.*, 2016, **2**, e1600225.

48 J. Shen, V. I. Hegde, J. He, Y. Xia and C. Wolverton, *Chem. Mater.*, 2021, **33**, 9486–9500.

49 I. G. Aleksandr, *Russ. Chem. Rev.*, 1988, **57**, 913.

50 Z. Wang, X.-G. Zhao, R. Koch, S. J. L. Billinge and A. Zunger, *Phys. Rev. B*, 2020, **102**, 235121.

51 I. K. Jeong, T. W. Darling, J. K. Lee, T. Proffen, R. H. Heffner, J. S. Park, K. S. Hong, W. Dmowski and T. Egami, *Phys. Rev. Lett.*, 2005, **94**, 147602.

52 J. C. Mikkelsen and J. B. Boyce, *Phys. Rev. Lett.*, 1982, **49**, 1412–1415.

53 A. Bianconi, N. L. Saini, A. Lanzara, M. Missori, T. Rossetti, H. Oyanagi, H. Yamaguchi, K. Oka and T. Ito, *Phys. Rev. Lett.*, 1996, **76**, 3412–3415.

54 X.-G. Zhao, G. M. Dalpian, Z. Wang and A. Zunger, *Phys. Rev. B*, 2020, **101**, 155137.

55 X.-G. Zhao, Z. Wang, O. I. Malyi and A. Zunger, *Mater. Today*, 2021, **49**, 107–122.

56 G. M. Dalpian, Q. Liu, J. Varignon, M. Bibes and A. Zunger, *Phys. Rev. B*, 2018, **98**, 075135.

57 L. Clark, J. Oró-Solé, K. S. Knight, A. Fuertes and J. P. Attfield, *Chem. Mater.*, 2013, **25**, 5004–5011.

58 B. Lu, C. B. Wahl, X. K. Lu, M. E. Sweers, H. Li, V. P. Dravid and L. C. Seitz, *J. Am. Chem. Soc.*, 2022, **144**, 13547–13555.

59 T. R. Welberry and B. D. Butler, *J. Appl. Crystallogr.*, 1994, **27**, 205–231.

60 J. Purans, A. Kuzmin, P. Parent and C. Laffon, *Electrochim. Acta*, 2001, **46**, 1973–1976.

61 J. Purans, A. Kuzmin, P. Parent and C. Laffone, *Ionics*, 1998, **4**, 101–105.

62 R. S. Singh and K. Maiti, *Phys. Rev. B: Condens. Matter Mater. Phys.*, 2007, **76**, 085102.

63 J. Wang, B. H. Toby, P. L. Lee, L. Ribaud, S. M. Antao, C. Kurtz, M. Ramanathan, R. B. Von Dreele and M. A. Beno, *Rev. Sci. Instrum.*, 2008, **79**, 085105.

64 P. L. Lee, D. Shu, M. Ramanathan, C. Preissner, J. Wang, M. A. Beno, R. B. Von Dreele, L. Ribaud, C. Kurtz, S. M. Antao, X. Jiao and B. H. Toby, *J. Synchrotron Radiat.*, 2008, **15**, 427–432.

65 L. R. Dalesio, J. O. Hill, M. Kraimer, S. Lewis, D. Murray, S. Hunt, W. Watson, M. Clausen and J. Dalesio, *Nucl. Instrum. Methods Phys. Res., Sect. A*, 1994, **352**, 179–184.

66 B. H. Toby and R. B. Von Dreele, *J. Appl. Crystallogr.*, 2013, **46**, 544–549.

67 A. Zunger, S. H. Wei, L. G. Ferreira and J. E. Bernard, *Phys. Rev. Lett.*, 1990, **65**, 353–356.

68 A. van de Walle, P. Tiwary, M. de Jong, D. L. Olmsted, M. Asta, A. Dick, D. Shin, Y. Wang, L. Q. Chen and Z. K. Liu, *Calphad*, 2013, **42**, 13–18.

69 M. Ångqvist, W. A. Muñoz, J. M. Rahm, E. Fransson, C. Durniak, P. Rozyczko, T. H. Rod and P. Erhart, *Adv. Theory Simul.*, 2019, **2**, 1900015.

70 A. van de Walle, *Calphad*, 2009, **33**, 266–278.

71 S. Kirklin, J. E. Saal, B. Meredig, A. Thompson, J. W. Doak, M. Aykol, S. Rühl and C. Wolverton, *npj Comput. Mater.*, 2015, **1**, 15010.

72 J. E. Saal, S. Kirklin, M. Aykol, B. Meredig and C. Wolverton, *JOM*, 2013, **65**, 1501–1509.

73 G. Kresse and J. Furthmüller, *Comput. Mater. Sci.*, 1996, **6**, 15–50.

74 G. Kresse and J. Furthmüller, *Phys. Rev. B: Condens. Matter Mater. Phys.*, 1996, **54**, 11169–11186.

75 G. Kresse and J. Hafner, *Phys. Rev. B: Condens. Matter Mater. Phys.*, 1993, **47**, 558–561.

76 P. E. Blöchl, *Phys. Rev. B: Condens. Matter Mater. Phys.*, 1994, **50**, 17953–17979.

77 G. Kresse and D. Joubert, *Phys. Rev. B: Condens. Matter Mater. Phys.*, 1999, **59**, 1758–1775.

78 J. P. Perdew, K. Burke and M. Ernzerhof, *Phys. Rev. Lett.*, 1996, **77**, 3865–3868.